Numerical simulations on thermocapillary migrations of nondeformable droplets with large Marangoni numbers

Zhaohua Yin, Lei Chang, Wenrui Hu, Qiaohong Li, and Hongyu Wang

Related Articles

Additional information on Phys. Fluids

Numerical simulations on thermocapillary migrations of nondeformable droplets with large Marangoni numbers

Zhaohua Yin,[1,a] Lei Chang,[1,b] Wenrui Hu,[1] Qiaohong Li,[1] and Hongyu Wang[2]

[1]*National Microgravity Laboratory, Institute of Mechanics, Chinese Academy of Sciences, Beijing 100190, People's Republic of China*
[2]*Anshan Normal University, Department of Physics, Liaoning 114005, People's Republic of China*

In this paper, the study on isolated spherical drops in thermocapillary migrations in zero gravity is carried out with a novel numerical scheme to accomplish long-tank simulations in a very short computing domain, and the full migrating phenomena with fairly large Marangoni numbers (up to 400) are discussed in detail. Larger Marangoni numbers lead to more complicated migrating processes, and longer distances for the drops to reach their final stable migrating velocities (U_F). There is nontrivial difference between the U_F values in theoretical analysis, numerical simulations, and space experiments, and the most possible reason is the assumed different migrating distances to reach steady states in different investigations. © *2012 American Institute of Physics*. [http://dx.doi.org/10.1063/1.4752028]

I. INTRODUCTION

In daily life and industrial production, there are often two or several mutually insoluble fluids mixed together to form droplets. In space, buoyancy effects can be ignored, so some other measures have to be introduced to drive drops, e.g., temperature effects, electromagnetic effects, and concentration effects. In particular, interfacial tensions normally decrease with increasing temperatures, the background liquid near the interface is driven toward the cold region, and the counterforce will push drops to the warm region. The drop migration caused by the temperature gradient on the interface is termed the thermocapillary migration.

In practice, it is convenient to assume that the density, (ρ), the kinematic viscosity, (μ), the thermal conductivity, (k), and the specific heat, (c_p) are constants. Hence, seven non-dimensional numbers in total are needed to describe the system, and a typical set is the following:

$$Ma = UR/\kappa_1,$$

$$Pr = \mu_1/(\rho_1\kappa_1),$$

$$Ca = \mu_1 U/\sigma_0,$$

$$\alpha = \mu_2/\mu_1,$$

$$\lambda = k_2/k_1,$$

$$\xi = \rho_2/\rho_1,$$

$$\gamma = c_{p2}/c_{p1}.$$

---

[a]Electronic mail: zhaohua.yin@imech.ac.cn.
[b]Present address: State Nuclear Power Technology R and D Center, Beijing, People's Republic of China.
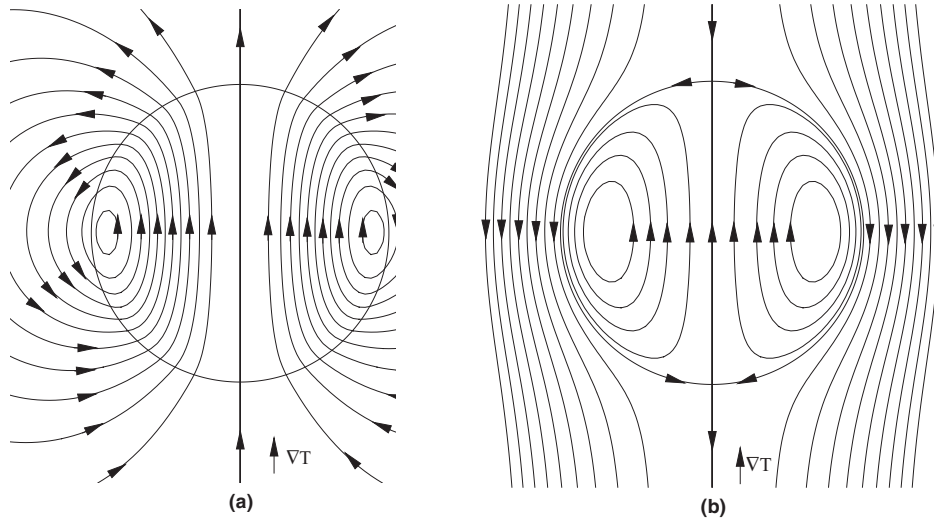
24, 092101-1

FIG. 1. The linearized analytical solutions of the thermocapillary flow.[2] (a) The streamlines in the laboratory coordinates, (b) the streamlines in a reference frame attached to the drop.

Here, R is the drop radius, $\kappa = k/\rho c_p$ the thermal diffusivity, and σ_0 the interface tension at a reference temperature T_0. Throughout this paper, symbols with subscript 2 are the parameters of the droplet/bubble, and those with the subscript 1 are the values of the bulk liquid. U is the reference velocity defined by the balance of thermocapillary force and viscosity force on the drop/bubble

$$U = |\sigma_T||\nabla T_\infty|R/\mu_1,$$

where σ_T is the changing rate of the interfacial tension with temperature, and ∇T_∞ the temperature gradient imposed on the bulk liquid. It is also common to adopt the Reynolds number ($Re = Ma/Pr$) instead of Pr in the above set.[1] In space experiments, the materials are fixed and Prs are constants. Thus, it is easier to compare numerical simulations with space experiments if Prs are fixed.

The original thermocapillary work by Young *et al.* neglected the inertial convection and thermal convection (the so-called *YGB* Model[2]), and the derived steady migration velocity is

$$V_{YGB} = \frac{2U}{(2 + 3\mu_2/\mu_1)(2 + k_2/k_1)}. \tag{1}$$

Moreover, the flow inside the drop forms a dipole as indicated in Fig. 1.

After YGB, there are many other studies on the thermocapillary motion of the isolated drop/bubble (see the review book[3]). According to the theoretical prediction in Ref. 4, the thickness of the temperature boundary layer along the interface is $O(1/\sqrt{Ma})$, which results in the main difficulties for those large Ma researches because the boundary layer is very thin.

Most investigations have so far concentrated on the system of the Fluorinert FC-75 drop and the silicone oil continuous phase. For small Ma numbers (<100), different studies reach a very good agreement: the final steady migrating speed of the drop (U_F) decreases with the increasing Ma number, and the related physical mechanism is discussed in details in Ref. 5. However, the U_F predictions diverge for those large Ma numbers (>100): the asymptotic analysis[4] and numerical simulations[6] showed that the U_F increases with the increasing Ma, but several space experiments showed that the U_F decreases with the increasing Ma.[7–9] So far as we know, there have been no studies that really reveal the full drop migrating process of large Ma numbers: some only worked on relatively small Ma numbers;[5] some focused on the final states;[6] and some worked on the first half process.[10] It has been predicted in Ref. 10 that the migrating distances to reach steady states for large Ma numbers are longer than the lengths of the experimental tanks, but so far, there have been no simulations providing any data of the necessary tank lengths, and the transient drop behaviours have never been fully studied. In addition, there are some phenomena observed in experiments,[8]
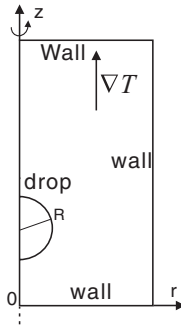
FIG. 2. The schematic diagram of the axisymmetric model for the Marangoni migration.

such as the "knee" in the plot of velocity of the drop against position for the larger drop (or the large Ma number), which require further discussions than that in Ref. 10. Therefore, it is necessary to investigate the drop's full migrating behavior with large Ma numbers, and this is the main focus of this work.

This paper is arranged as follows: the governing equations and numerical methods are introduced in Sec. II, efforts to overcome the numerical difficulties of large Ma numbers are presented in Sec. III, and the results and discussions are in Sec. IV.

II. GOVERNING EQUATIONS

In this study, the axisymmetric model is adopted to perform high resolution simulations (Fig. 2). The drop with the radius R is surrounded by the bulk fluid in a cylinder $\Omega = [0, r_1] \times [z_0, z_1]$. The direction of the temperature gradient is along the z-axis. The front-tracking method is employed in our simulations, and by connecting the material parameters of two liquids with a smooth function,[11] the governing equations for the entire domain can be written as

$$\nabla \cdot \mathbf{u} = 0, \tag{2}$$

$$\frac{\partial(\rho \mathbf{u})}{\partial t} + \nabla \cdot (\rho \mathbf{u}\mathbf{u}) = -\nabla p + \nabla \cdot (\mu(\nabla \mathbf{u} + \nabla^T \mathbf{u})) + \boldsymbol{F}_\sigma, \tag{3}$$

$$\rho C_P(\frac{\partial T}{\partial t} + \mathbf{u} \cdot \nabla T) = \nabla \cdot (k\nabla T). \tag{4}$$

Here, $\mathbf{u} = (u, w)$ is the velocity vector, p the pressure, and T the temperature. $\boldsymbol{F}_\sigma$ is the body force term produced by the interfacial tension

$$\mathbf{F}_\sigma = \int_B \delta(\mathbf{x} - \mathbf{x}_f)(\sigma \zeta \mathbf{n} + \frac{\partial \sigma}{\partial s}\boldsymbol{\tau})ds, \tag{5}$$

where $\mathbf{x} = (r, z)$ is the space vector, $\mathbf{x}_f = (r_f, z_f)$ the position of the cell f on the interface B, δ a delta function, σ the interfacial tension, ζ the sum of two principal curvatures of the interface, and s the natural coordinate along the interface. $\mathbf{n} = (n_r, n_z)$ and $\boldsymbol{\tau}$ denote the normal and tangential unit vectors of the interface, respectively.

The nondimensional quantities are defined as

$$\bar{\mathbf{u}} = (\bar{u}, \bar{w}) = \mathbf{u}/U, \quad \bar{\mathbf{x}} = (\bar{r}, \bar{z}) = \mathbf{x}/R, \quad \bar{t} = t/(\frac{R}{U}),$$

$$\bar{p} = p/(\rho_1 U^2), \bar{\rho} = \rho/\rho_1, \quad \bar{\mu} = \mu/\mu_1, \quad \bar{k} = k/k_1, \tag{6}$$

$$\bar{C}_p = C_p/C_{p1}, \quad \bar{T} = T/(|\nabla T|R), \quad \bar{\boldsymbol{F}}_\sigma = \boldsymbol{F}_\sigma R/(\rho_1 U^2).$$

Thus, we have the non-dimensional equations

$$\nabla \cdot \bar{\mathbf{u}} = 0, \tag{7}$$

$$\frac{\partial(\bar{\rho}\bar{\mathbf{u}})}{\partial \bar{t}} + \nabla \cdot (\bar{\rho}\bar{\mathbf{u}}\bar{\mathbf{u}}) = -\nabla \bar{p} + \frac{1}{Re}\nabla \cdot (\bar{\mu}(\nabla \bar{\mathbf{u}} + \nabla^T \bar{\mathbf{u}})) + \bar{\mathbf{F}}_\sigma, \tag{8}$$

$$\bar{\rho}\bar{C}_p\left(\frac{\partial \bar{T}}{\partial t} + \bar{\mathbf{u}} \cdot \nabla \bar{T}\right) = \frac{1}{Ma}\nabla \cdot (\bar{k}\nabla \bar{T}). \tag{9}$$

Boundary conditions on the solid walls (Fig. 2) are

$$\begin{aligned}
\bar{u}|_{\bar{r}=\bar{r}_1} &= \bar{u}|_{\bar{z}=\bar{z}_0, \bar{z}_1} = 0, \\
\bar{w}|_{\bar{r}=\bar{r}_1} &= \bar{w}|_{\bar{z}=\bar{z}_0, \bar{z}_1} = 0, \\
\bar{T}|_{\bar{r}=\bar{r}_1} &= \bar{T}_0 + \bar{z}, \\
\bar{T}|_{\bar{z}=\bar{z}_0} &= \bar{T}_0 + \bar{z}_0, \\
\bar{T}|_{\bar{z}=\bar{z}_1} &= \bar{T}_0 + \bar{z}_1.
\end{aligned} \tag{10}$$

Boundary conditions on the symmetry axis are

$$\bar{u}|_{\bar{r}=0} = 0, \quad \frac{\partial \bar{w}}{\partial \bar{r}}\Big|_{\bar{r}=0} = 0, \quad \frac{\partial \bar{T}}{\partial \bar{r}}\Big|_{\bar{r}=0} = 0. \tag{11}$$

It is difficult to have the same initial conditions as those in experiments,[1] so we stick to the traditional ones

$$\begin{aligned}
\bar{u}|_{\bar{t}=0} &= \bar{w}|_{\bar{t}=0} = 0, \\
\bar{T}|_{\bar{t}=0} &= \bar{T}_0 + \bar{z}.
\end{aligned} \tag{12}$$

In the following, symbols without bars are adopted to indicate nondimensional values (except Sec. IV C, where the experimental data are discussed and compared with those of the simulations). The physical parameters are: $Pr = 83.3, \alpha = 0.14, \lambda = 0.47, \xi = 1.89, \gamma = 0.69$, and $Ca = 0.04$, so the results can be roughly compared with the Life and Microgravity Science (LMS) space experiments.[8]

III. NUMERICAL DIFFICULTIES IN SIMULATIONS WITH LARGE MA NUMBERS AND COUNTERMEASURES

Compared with those studies of small Ma numbers, there are two major difficulties in numerical simulations with strong thermal convections:

1. The migrating process is more complicated, and much longer time and larger domain are needed for the drop to reach U_F. For example, the drop needs to migrate a distance of 90R to reach the steady state for $Ma = 300$ (see Fig. 14(b)).
2. Boundary layers are very thin for large Ma numbers ($1/\sqrt{Ma}$,[4]), and require very fine resolutions.

A. The countermeasure for the first difficulty: The dynamic computing domain

The simplest solution to deal with the first difficulty is to adopt a very long tank in simulations ($>10R$). However, most computing time is wasted in this strategy because the regions far away from the drop (roughly $0.5 \sim 1R$ above the drop and $2 \sim 3R$ behind the drop) are trivial in our studies.

Another typical solution is to perform simulations on the reference frame attached to the drop instead of in the laboratory coordinates.[6] The merit of this strategy is that no moving interface exists in simulations, and that various computational techniques such as body-fitting grids and adaptive
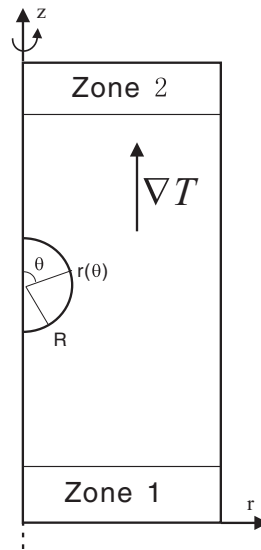
FIG. 3. The schematic diagram of the dynamic domain.

grids can be adopted to reach an effective high local resolution near the interface; thus, no intensive computation is needed. The drawback is also clear: only the final steady state can be studied, and the transient migrating behavior remains unrevealed.

Our strategy is a trade-off between the above two solutions: the laboratory coordinate is adopted and the computing domain is kept as short as possible. The drop starts from a position just above the cold wall. When the drop migrates near the hot wall, the computing domain near the cold wall (Fig. 3, Zone 1) is then removed, and Zone 2 with the same size of Zone 1 is patched above the hot wall. The initial data in Zone 2 are the undisturbed ones (Eq. (12)). The above procedure is repeated until a steady migrating state is reached.

Figure 4 illustrates a validating test for this dynamic domain. The benchmark simulation adopts the static long-tank domain ($4R \times 60R$), and the size of the dynamic domain is $4R \times 16R$. It seems that the velocity difference between these two simulations is trivial, while the static domain is almost four times as large as the dynamic one.

B. The countermeasure for the second difficulty: The pressure equation solver based on the standard Poisson equation solver

In the current numerical scheme, the most time-consuming part is to solve the pressure equation derived in the projection Method[12]

$$\nabla(\frac{1}{\rho^{n+1}}\nabla p^{n+1}) = \nabla \cdot (\mathbf{u}^*)^n, \tag{13}$$

with the Neumann boundary conditions[11, 13]

$$\frac{\partial p}{\partial r}\big|_{r=0,r_1} = \frac{\partial p}{\partial z}\big|_{z=z_0,z_1} = 0,$$

where n is the time step, and $\mathbf{u}^*$ the intermediate velocity.

Typical methods to solve the above equations are the successive over-relaxation (SOR) method and the multi-grid method, but it is not so easy to parallelize these two methods. For the standard Poisson equation, however, there are more choices available: the cyclic reduction method[14, 15] and the schemes based on fast Fourier transform (FFT).[16, 17] Based on these standard Poisson solvers, it
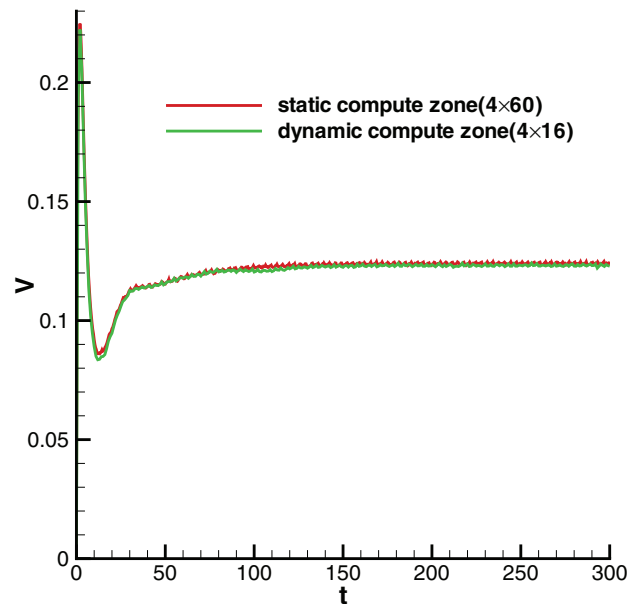
FIG. 4. Time evolutions of drop velocities calculated by the static domain and the dynamic domain for Ma = 100. Twenty-five grids are adopted per radius.

is also possible to solve the pressure equation with an iterative method[18]

$$\Delta p^{n+1} = -\rho^n \nabla(\frac{1}{\rho^n}) \cdot \nabla p^n + \frac{\rho^n}{\Delta t} \nabla \cdot (\mathbf{u}^*)^n. \tag{14}$$

In this paper, the strategies on the basis of FFTs (Tri-FFT) are adopted to solve the standard Poisson equation so that we can take advantage of the global efforts to fasten FFTs. So far as we know, the technical details for the axisymmetric Tri-FFT model with Neumann boundary conditions have never been discussed in any earlier literatures, so they are presented in the Appendix. Due to the efficiency of available FFT algorithms, this scheme is about twenty times faster than the SOR methods for the finest simulation in this research.

Moreover, the above scheme can eliminate the side-effect caused by the dynamic computing domain described in Subsection III A since it is not sensitive to initial conditions. Generally speaking, $6 - 7$ iterations of Eq. (14) are enough to reach the convergence of the pressure equation. On the other hand, the SOR scheme requires $10 - 10^5$ iterations depending on good or poor initial conditions. It is clear that the dynamic domain will lead to poor initial conditions when the domain is adjusted, but it does not lead to longer computing time for the current solver.

It is worth mentioning that there is no solid mathematical proof to guarantee the convergence of Eq. (14) for all pressure equations, although it does converge for our incompressible two-phase flow with interfaces far away from physical boundaries.

IV. THE THERMOCAPILLARY MIGRATION OF A SINGLE DROP WITH STRONG THERMAL CONVECTION

Throughout this study, the time step is 5×10^{-5}, the dynamic domain $4R \times 16R$, and the resolution 200×800.

A. Thermocapillary migrations of drops with different Ma numbers: A first view

In this subsection, seven Ma numbers are adopted in simulations, and the normalized velocities (V/V_{YGB}) are shown in Fig. 5. All simulations have reached their final steady migration states. When Ma is relatively small ($Ma < 100$), the U_F decreases as Ma increases. When Ma is fairly
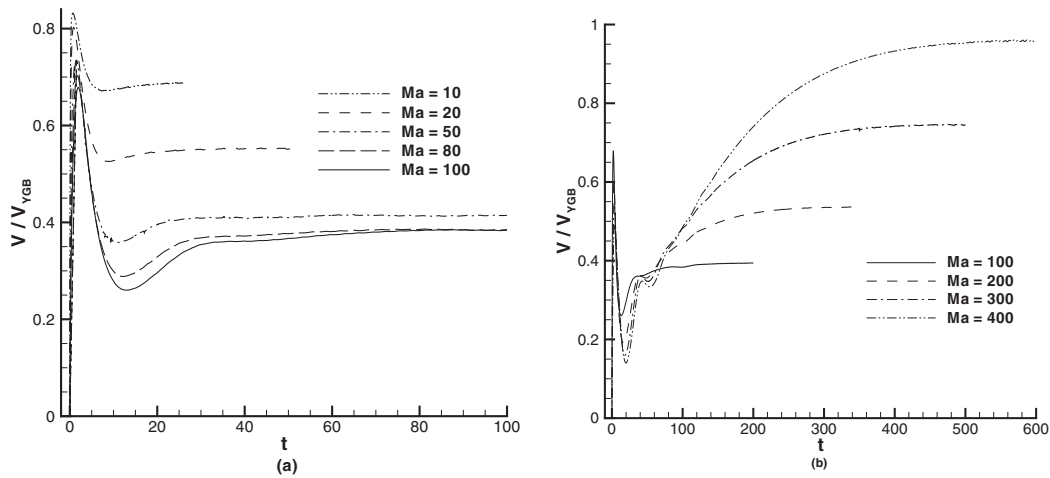
FIG. 5. Time evolutions of drop migration velocities with different *Ma* numbers. (a) *Ma* = 10; 20; 50; 80; 100. (b) *Ma* = 100; 200; 300; 400.

large (*Ma* > 100), the U_F increases with Ma. This is consistent with the result of previous numerical simulations.[6]

When the thermal convection is very weak (*Ma* ≈ 0), there are only two stages for the time evolution of the migration velocity: the beginning accelerating stage and the final steady migration stage.

When the thermal convection becomes stronger (10 < *Ma* < 100, see Fig. 5(a)), there is a new stage besides the above two: the overshoot stage. The overshoot stage occurs at the beginning of the whole process due to the redistribution of the temperature field inside the drop because the influence of the thermal convection is stronger than that of the heat diffusion. The detailed discussion of this phenomenon can be found in many previous works.[1,5]

When the thermal convection becomes even stronger (*Ma* ≥ 200), the migrating process becomes more complicated, and there are five stages involved (Fig. 6):

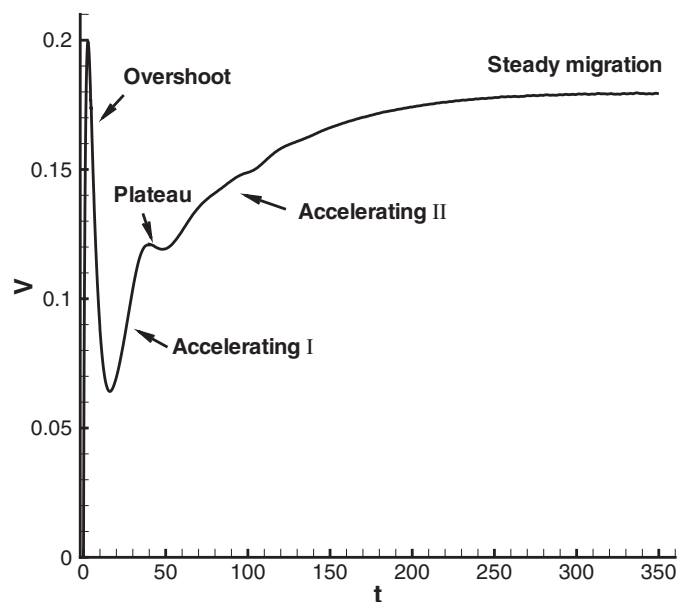1. the "overshoot" stage;

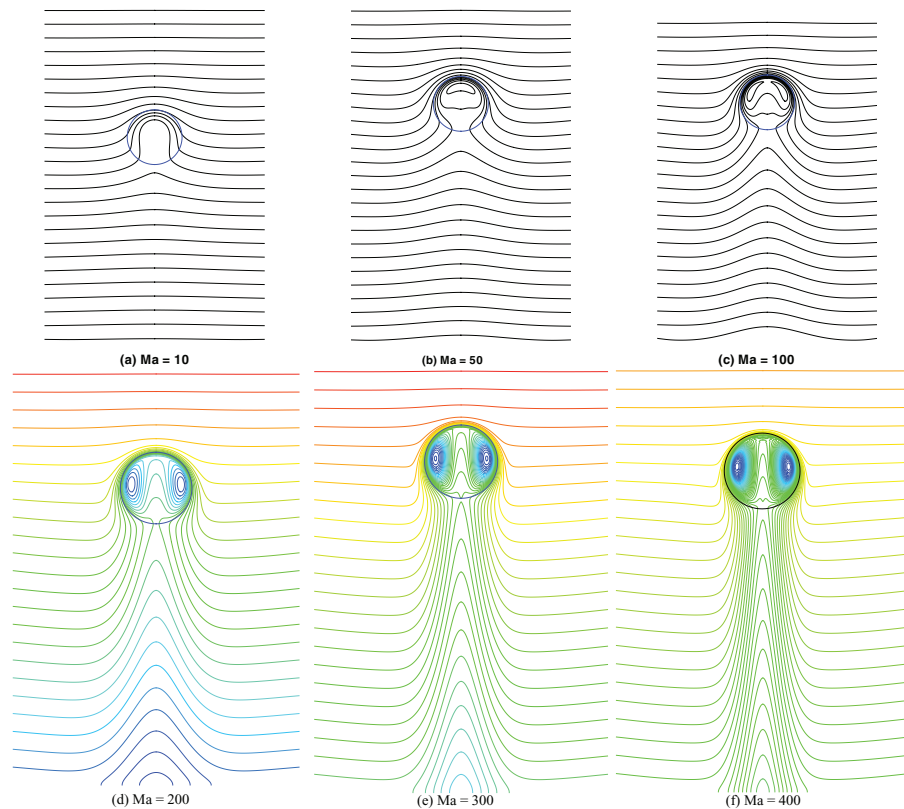FIG. 6. Five stages of the drop migration velocity with *Ma* = 200.

FIG. 7. Temperature contours when drops reach their final migration states. The temperature difference between nearby contours is 0.5. (a) Ma = 10. (b) Ma = 50. (c) Ma = 100. (d) Ma = 200. (e) Ma = 300. (f) Ma = 400.

2.   the first acceleration stage (Accelerating I);
3.   the "plateau" stage;
4.   the second acceleration stage (Accelerating II);
5.   the final steady migration stage.

Figure 7 presents the isotherms of steady migration states for different Ma numbers. From small Ma numbers, the isotherms just above the drop begin to bend and embrace the drop, and the larger Ma number is, the more part of the drop is enwrapped. When $Ma = 50$, some cold fluid originally near the bottom of the drop is transported to the drop center before heated up by the surroundings. As a result, the "cold region" is formed. With even larger Ma numbers, the cold region expands and moves toward the boundary near the front stagnation point. When $Ma > 100$, the "cold region" near the axis is empty and a "cold ring" appears.

To sum up, there are mainly two mechanisms that influence the U_F:

• For increasing Ma numbers, the bending of the isotherms just above the drop reduces the temperature gradient along the interface;
• For the stronger thermal convection, the "cold region" is closer to the interface. As a result, the temperature boundary layer near the interface becomes stronger, and the isotherms there are more compact. So, the interfacial temperature gradient near the drop bottom becomes larger.

It is obvious that the first mechanism makes the driving force on the drop smaller because the gradient of the capillary force along the interface becomes smaller; and the second mechanism makes the drop move faster.

When the Ma number increases from 10 to 50, the temperature gradient along the interface decreases because of the first mechanism (Figs. 7(a) and 7(b)), and the influence of the second mechanism is not obvious yet. For $Ma > 50$, the influence of the first mechanism does not become
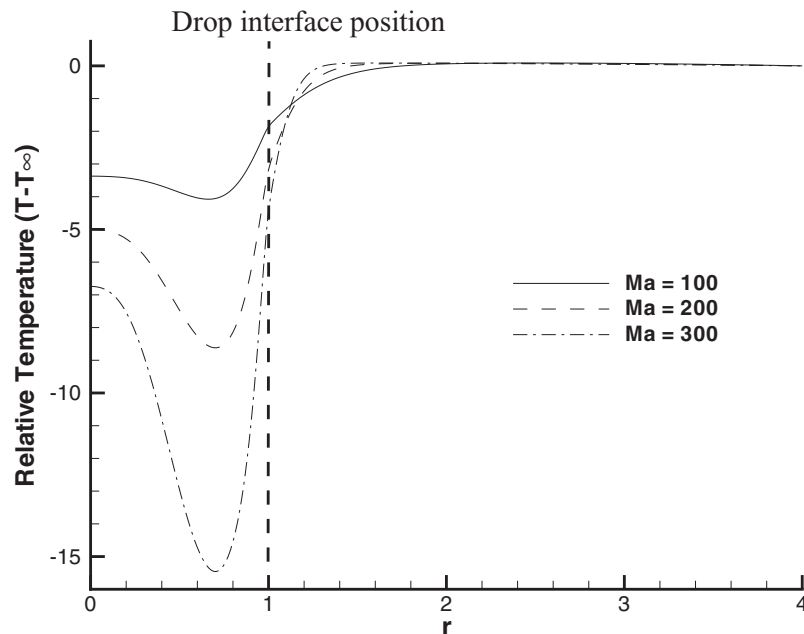
FIG. 8. Relative temperature distribution along the horizontal line through the drop center when the drop reaches its steady migration state. T_∞ is the temperature on the solid wall in the same horizontal line.

much stronger for the larger *Ma*, and the second mechanism begins to take effect. From $Ma = 50$ to $Ma = 100$, the interfacial temperature gradient on the upper half of the drop only experiences slight changes, but that on the lower half obviously keeps increasing (Figs. 7(b) and 7(c)). Consequently, the U_F decreases quickly for larger Ma numbers before $Ma = 50$, but falls slowly for $Ma > 50$, and this decrease stops around $Ma = 100$ (Fig. 5(a)).

From $Ma = 100$ to 400, the "cold ring" expands and moves from the front stagnation point to the equator of the drop (Figs. 7(c)–7(e)). Due to stronger thermal convections, the heat-up of the cold fluid is slower for larger Ma numbers, and the relative temperature in the "cold ring" is also lower. As indicated in Fig. 8, the coldest point on the "cold ring" is 8.5 lower than T_∞ with $Ma = 200$, and 15.5 lower with $Ma = 300$. The scaled temperature distribution along the interface shows that the temperature difference between the stagnation points becomes larger for a larger Ma (Fig. 9). This leads to the stronger temperature boundary layer, the denser isotherms inside the drop, the larger interfacial temperature gradient near the drop bottom, and eventually the obvious increase in U_F (Fig. 5(b)).

B. The full process of the large-Ma thermocapillary migration

In this subsection, we attempt to focus the analysis on the full migrating process with strong thermal convection.

Figure 10 shows the temperature field near the droplet for different times with $Ma = 200$. Right after the beginning of the simulation, the originally straight isotherms just above the drop start to bend and embrace the drop. At $t \approx 20$, some cold fluid originally near the bottom of the drop is transported to the drop center before heated up by the surroundings, and the "cold region" thus take form. Later, the "cold region" expands and moves toward the boundary near the front stagnation point. Around $t = 40$, the part of the "cold region" near the axis becomes relatively hotter, and a "cold ring" appears.

Similar to the two mechanisms on the U_F in Subsection IV A, there are also two main mechanisms that influence the temporary migrating velocity of the drop:

- As time goes on, the bending of the isotherms just above the drop reduces the interfacial temperature gradient near the top of the drop;
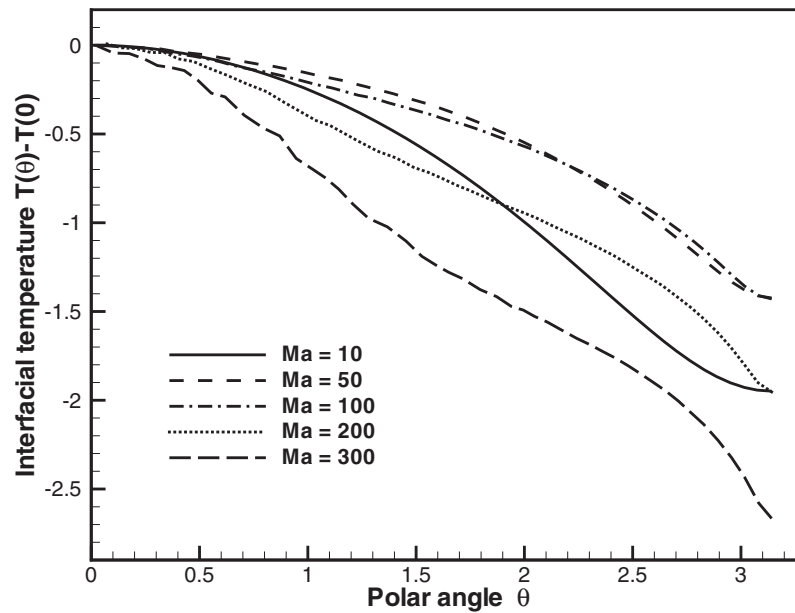
FIG. 9. Scaled temperature distribution along the drop interface for various Ma numbers. θ is defined as the angle from the interface to the drop center. $\theta = 0$ corresponds to the top of the drop, and $\theta = \pi$ to the bottom of the drop.

- At the later time of the simulation, the "cold region" is closer to the interface, so the temperature boundary layer near the interface becomes stronger. As a result, the isotherms there are more compact, and eventually the interfacial temperature gradient near the drop bottom becomes larger.
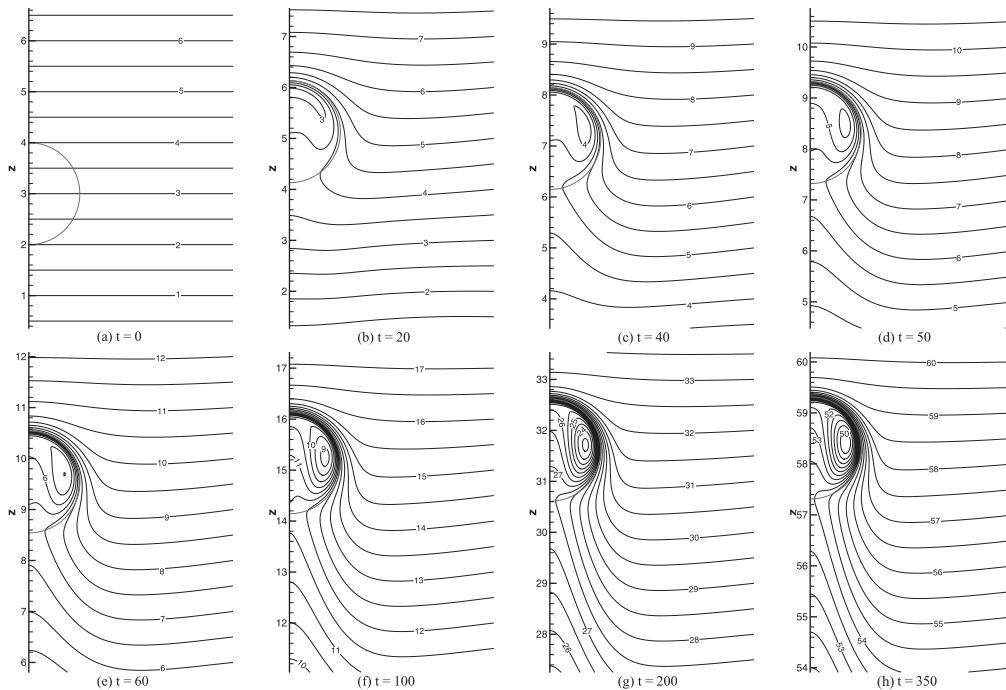

FIG. 10. Temperature contours at different times with Ma = 200. (a) t = 0. (b) t = 20. (c) t = 40. (d) t = 50. (e) t = 60. (f) t = 100 (g) t = 200 (h) t = 350.
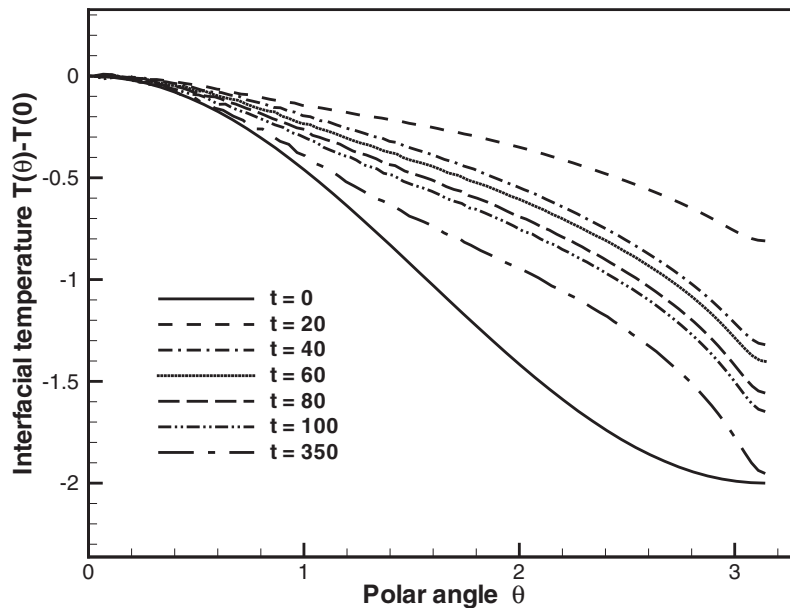
FIG. 11. Scaled temperature distribution along the drop interface for $Ma = 200$. See the definition of θ in the caption of Fig. 9. (Note: The lowest curve corresponds to $t = 0$; and for all other curves (namely, $t > 0$), the curve of the later time is in a lower position.)

From $t = 0$ to $t = 20$, the first mechanism significantly reduces the temperature gradient along the interface. This can be seen clearly in Fig. 11 since the $t = 20$ curve is in the highest position while the $t = 0$ curve is in the lowest one.

After $t = 40$, the influence of the second mechanism starts to become obvious, so the relative temperature of the "cold ring" becomes even lower (Fig. 12). Hence, generally speaking, after the "overshoot" stage, the drop velocity keeps increasing till the final steady state (Fig. 6). An
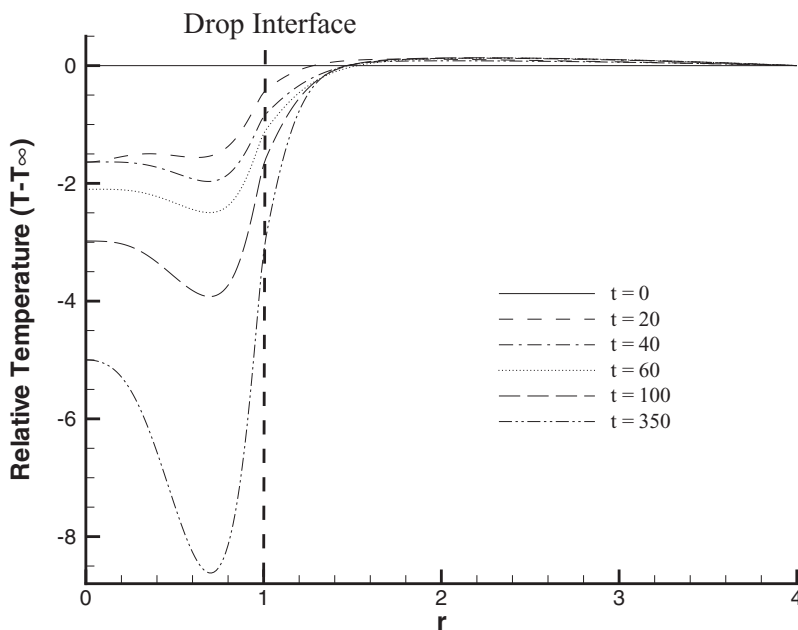

FIG. 12. Relative temperature distribution along the horizontal line through the drop center for different times of the $Ma = 200$ run.
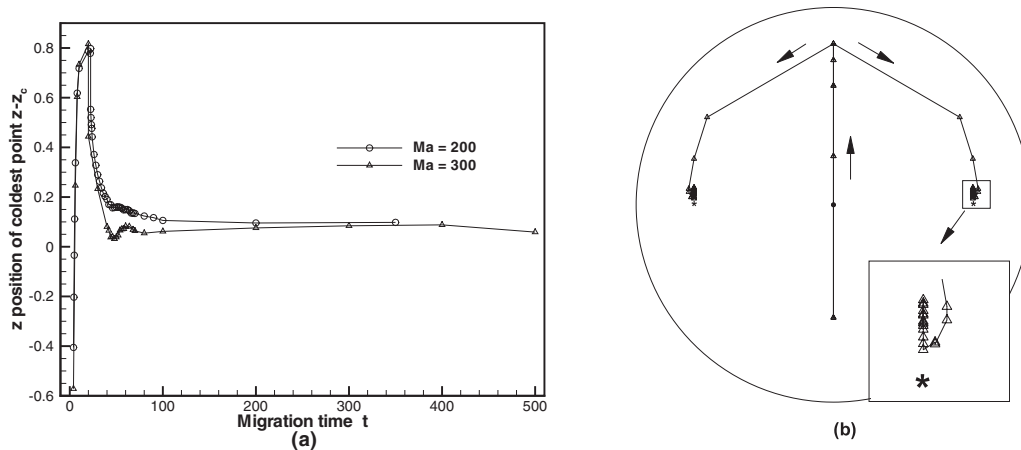
FIG. 13. Locations of the coldest points inside drops: (a) time evolutions of z coordinates with $Ma = 200$ and 300; (b) the locus with $Ma = 300$.

exception is the "plateau" stage, when two mechanisms try to find a balance between themselves. To be more specific, when $t \in [40, 60]$, the temperature boundary layer is not fully developed yet (Figs. 10(c)–10(e)), and the heating-up of the "cold ring" by the heat diffusion is in the same order as the cooling-down by the thermal convection.

Another interesting phenomenon during the "plateau" stage is the locus of the coldest point inside the drop (Fig. 13). At first, the coldest point moves up from the bottom of the drop along the $r = 0$ line, and then it falls apart from the symmetric axis when the "cold ring" starts to appear. If we focus on the time evolution of the z coordinate of the coldest point, there is a small overshoot around $t = 40 \sim 60$ after the big one (Fig. 13(a)). The second overshoot is more obvious for the $Ma = 300$ run. A simple comparison between Figs. 13(a) and 5(b) reveals that the second overshoot and the "plateau" stage occur simultaneously. Table I presents the detailed coordinates of the coldest point around the "plateau" stage for $Ma = 300$. It is clear that, after $t = 40$, the coldest point paces up and down before moving towards its destination (see the drawing of partial enlargement in Fig. 13(b)).

After the "plateau" stage, the temperature boundary layer gradually becomes fully developed, the "cold ring" becomes colder, the interfacial temperature gradient near the drop bottom becomes larger, and the drop velocity is in the second acceleration stage. Finally, there is a balance between the thermal diffusion and convection, and the final steady migration state is reached.

C. The comparison between our numerical simulations and space experiments

Before any comparison is made, it is convenient to list the assumptions adopted in our simulations:

1. The existence of the "overshoot" stage:
   In our previous investigation,[1] it has been analyzed that the current initial condition induces the "overshoot" phenomenon of the velocity, and the "overshoot" stage will not be so obvious in real experiments.
2. The temperature-independent viscosity and density:
   It has been clarified that this assumption leads to nontrivial difference from the space experiments.[5, 10]
3. Trivial drop deformation:

TABLE I. Coordinates of the coldest point at $t = 40 \sim 60$ with $Ma = 300$. The droplet center is at (r_c, z_c).

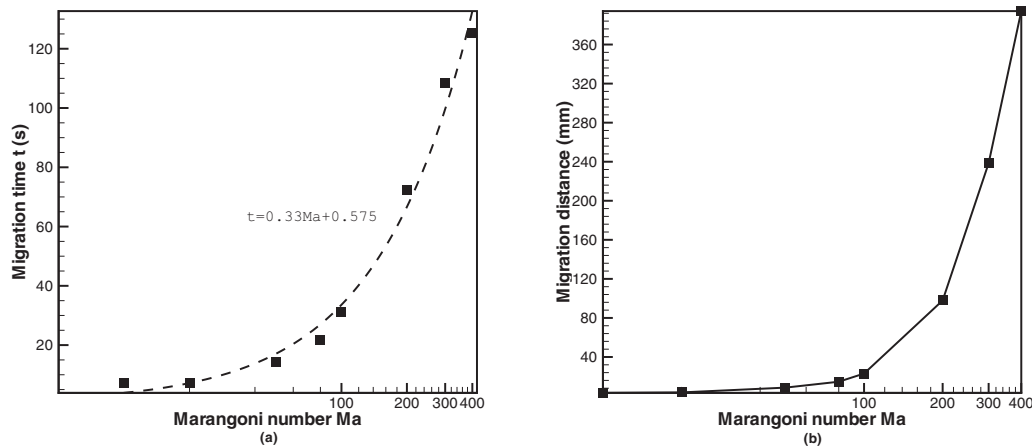| Time	40	42	44	46	48	50	52	54	56	58	60
r	0.73	0.73	0.72	0.72	0.71	0.71	0.71	0.71	0.71	0.71	0.71
$z - z_c$	0.081	0.065	0.038	0.040	0.032	0.039	0.0469	0.066	0.071	0.072	0.083

FIG. 14. Dimensional times and distances required for the drop to reach final steady states for different *Ma* numbers. (a) *Ma* numbers vs. migration time. (b) *Ma* numbers vs. migration distance.

According to Ref. 19, the simulation must be stopped before the drop center migrates a distance much shorter than $(1/Ca - 1)R$ in the z direction to avoid the noticeable deformation. However, in this paper, $(1/Ca - 1)R = 24R$ is not enough for those $Ma \geq 200$ runs to reach their final migration states.

We stick to the above assumptions because they have been widely employed in most previous analytical and numerical studies,[1–4, 6] and it will be seen later in this subsection that our simulations can still give a pretty good explanation for most experimental phenomena.

If only the last four stages in Fig. 6 are considered, we will find a very good agreement with the LMS space experiment. In particular, Fig. (4b) in Ref. 8 shows the existence of the "knee" in the plot of velocity of the drop against position for the larger drop, and the "knee" lasts about 5 s. Using the material parameters at $T = 30\,^\circ$C ($\sigma_T = -0.036$ mN/mK and $|\nabla T_\infty| = 1$K/mm), the nondimensional "knee" time can be calculated by the expression $t|\sigma_T||\nabla T_\infty|/\mu_1 = 20.7$. It is clear that the "plateau" stage in our simulation lasts roughly as long as that of the experiments.

Figure 14 shows the dimensional times and distances needed by the drop to reach its final steady states based on our simulations. It is obvious that the required time and distance increase with the Ma number. The least square fit shows that the required dimensional time of large *Ma* numbers follows the expression

$$t = 0.33Ma + 0.575(s), \tag{15}$$

and the coefficient of determination $E^2 = 0.98$. The previous research[8] adopts a different expression based on the linear analytical result of Kronig and Brink[20]

$$t = 0.0096R^2/\kappa_2. \tag{16}$$

There is a big gap between the above two expressions when Ma numbers are fairly large. For example, when Ma = 200, the radius of the FC-75 droplet is 2.04 mm, and the thermal diffusivity is $\kappa_2 = 0.034$ mm^2/s. So, the time for the drop to reach the steady state determined by Eq. (16) is 11.8 s, while it is about 70 s according to Eq. (15). Moreover, the length of the tank in the LMS space experiment is 60 mm, which is not long enough for large drops to reach their steady migration states according to our numerical simulations: the tank should be longer than 93 mm for Ma = 200 and 238 mm for Ma = 300.

The U_Fs from previous studies are summed up in Fig. 15. The results of our simulations are close to those of the steady simulations in Ref. 6, but are quite different from the space experiment results. To be specific, the numerical results (this work and Ref. 6) agree with the findings of the space experiments for $Ma < 100$, but they become larger than experimental data after $Ma > 100$. The asymptotic result[4] shows a similar trend to the numerical prediction for large *Ma* numbers.
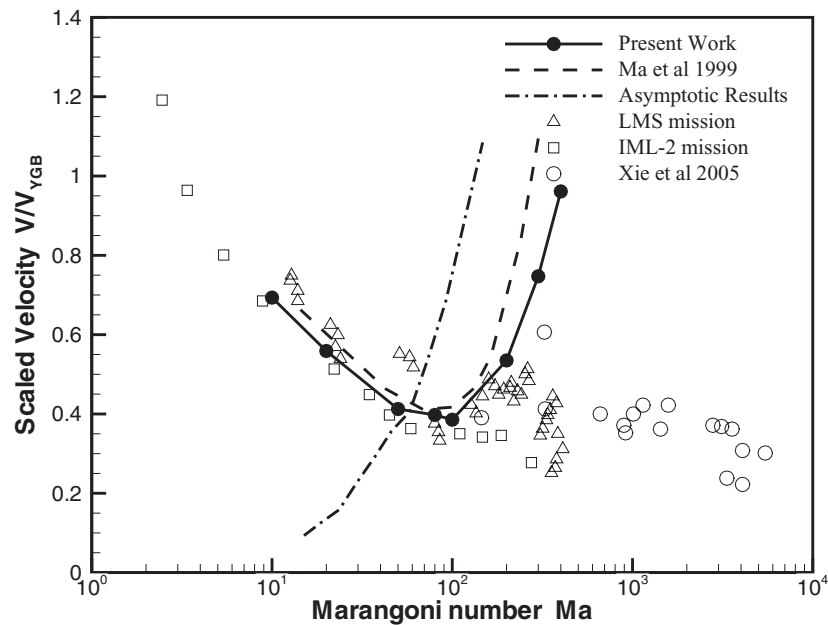
FIG. 15. The resulted U_Fs from the asymptotic theory, numerical simulations, and space experiments.

The main reason bringing the difference in U_Fs is the long complex migration process for large Ma numbers, so it is impossible for the space experiments to observe the final steady migration state within a short tank of 60 mm.

In the space experiments, all data are taken within approximate 10 mm of traverse distance in the tank.[8] To get a direct comparison, we replace the U_Fs with the drop speeds at $z = 25$ mm and 35 mm in our simulations. The resulting data are plotted in Fig. 16, and a fairly good agreement with the space experiments is reached. It is interesting that the sampled velocity for $Ma = 400$ at $z = 35$ mm
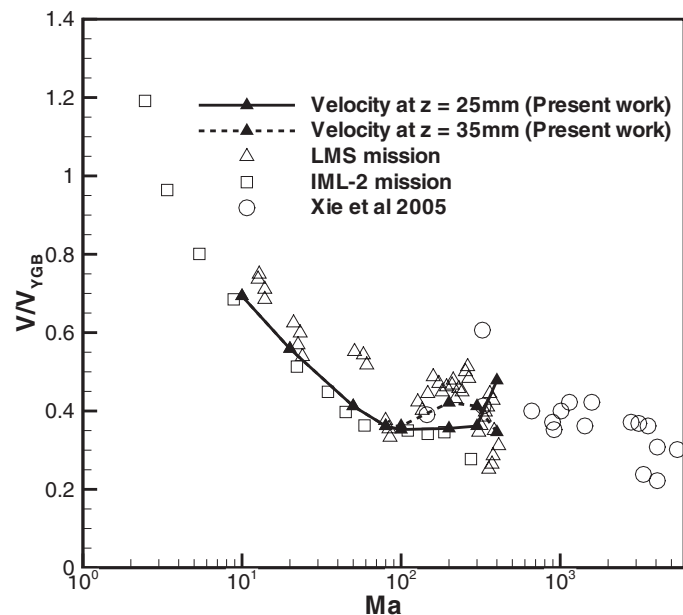

FIG. 16. The intermediate drop velocities at $z = 25$ and 35 mm from our numerical simulations and the corresponding experimental results.
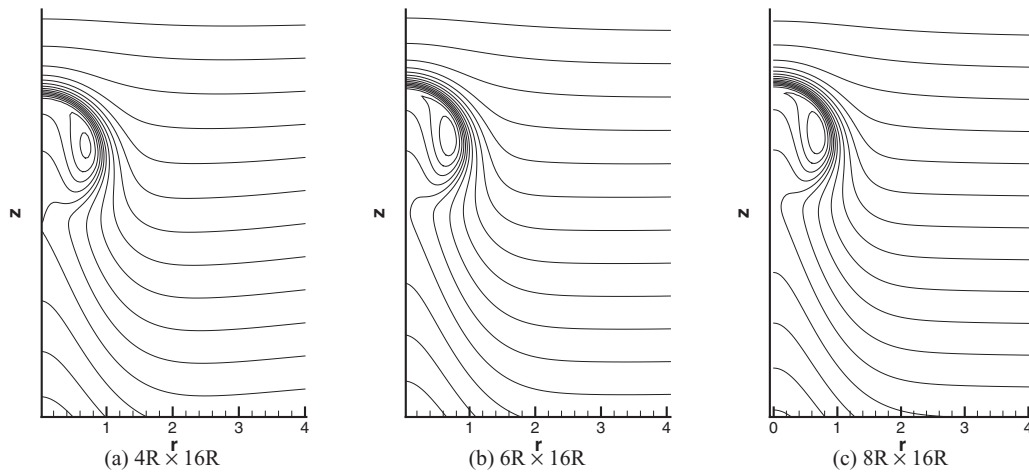
FIG. 17. Temperature contours when drops reach their final migration states with different domain widths for $Ma = 150$.

is lower than that of $Ma = 300$ because: (1) the first three stages defined in Fig. 6 last longer for larger Ma numbers (see Fig. 5); (2) $Ma = UR/\kappa_1$ means that a larger Ma number corresponds to a larger drop, which means that the first three stages in Fig. 6 cover longer physical distance. It also explains why the sampled experimental velocities for $Ma > 500$ are even lower (see Fig. 6 and Ref. 9).

It is worth mentioning that all experimental data are sampled when drops migrate a distance shorter than 20 mm from the injection needle, or the effective maximum temperature difference in the system is 20K. Therefore, the comparison in Fig. 16 roughly meets the requirement of the Boussinesq approximation in our simulations.

D. The influence of the domain width

In our simulations, the domain width is fixed at 4R, while in the experiments it varies from $3R \sim 24R$ (note that the axisymmetric coordinate is adopted here). Since the cylinder is confined on top
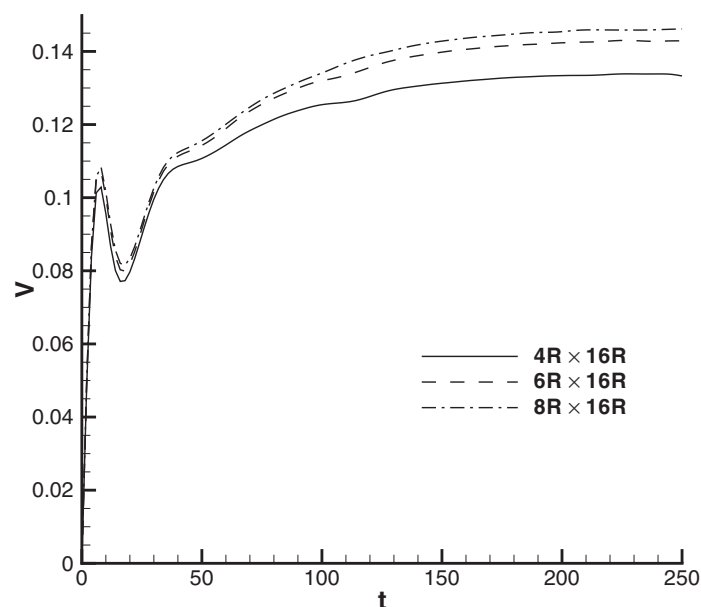

FIG. 18. Time evolutions of drop migration velocities with different domain widths for $Ma = 150$.

and bottom, there should be a back flow in the outer fluid. To provide a better support for the future experiments, it is necessary to consider the influence of the domain widths in numerical simulations.

From Fig. 17, we can see that the different domain widths lead to nearly the same final-state temperature contours for $Ma = 150$. On the other hand, although the migrating velocities roughly experience the same five stages as those defined in Sec. IV A, there is obvious difference in the U_F values (Fig. 18). Similar conclusions were reached in a level-set simulation.[10]

V. CONCLUSIONS

In this paper, we develop an efficient numerical solver to investigate the drop thermocapillary migrations with large Ma numbers. The dynamic adjustment of the computing domain can significantly reduce the total resolution, and the iteration scheme based on the tri-FFT can solve the pressure equation much faster than the traditional ones.

The different migration processes of drops with various Ma numbers are discussed. A larger Ma number leads to a more complicated process, longer time, and larger distance for the droplet to reach the final steady state. In our simulations, the sharp interface numerical scheme is adopted. Although this brings some difficulties in programming,[21] it leads to a better observation of the "plateau" stage, and a very good agreement of our simulations with the space experiments.

In addition, the different U_Fs predicted by different investigations are compared, and the major reason leading to the divergence in various predictions is the underestimation of the drop's migrating distance to reach its final steady state for large Ma numbers.

Finally, some suggestions for future experiments can be made. The necessary tank length according to our work is significantly longer than that of any earlier predictions. So, if the goal of experiments is related to the final steady migrating velocity with large Ma numbers, at least one of the following strategies should be considered:

- Extend the physical length of the current tank. The extension should go along with the decrease of the temperature on the cold wall instead of the increase of the temperature on the hot wall, because the temperature on the hot wall of current experiments is already close to the burning point of the silicone oil;
- Extend the nondimensional length of the tank by using different experimental liquids (other than the Fluorinert FC-75 drop and the silicone oil continuous phase) to make drops smaller while keeping the Ma number big enough.

ACKNOWLEDGMENTS

APPENDIX: THE TRI-FFT POISSON SOLVER WITH NEUMANN BOUNDARY CONDITION IN AXISYMMETRICAL MODEL

The details of the Poisson solver can be found in Refs. 22 and 23, and only some specifics of the solver about the Neumann boundary condition in axisymmetrical model are presented here. With the three-point centered finite-difference method, the axisymmetrical poisson equation discreted on a uniform, Cartesian, staggered grid can be written as

$$a_i \mathbf{X}_{i-1} + b_i \mathbf{X}_i + c_i \mathbf{X}_{i+1} + A \mathbf{X}_i = \mathbf{D}_i,$$

$$\mathbf{X}_i = \{p_{i,1}, p_{i,2}, ..., p_{i,N_z}\}^T, \tag{A1}$$

$$\mathbf{D}_i = \Delta z^2 \{d_{i,1}, d_{i,2}, ..., d_{i,N_z}\}^T,$$

$$A = \begin{pmatrix} 1 & -1 & 0 & \cdots & \cdots & \cdots \\ -1 & 2 & -1 & 0 & \cdots & \cdots \\ \cdots & \cdots & \cdots & \cdots & \cdots & \cdots \\ \cdots & \cdots & \cdots & \cdots & \cdots & \cdots \\ \cdots & \cdots & 0 & -1 & 2 & -1 \\ \cdots & \cdots & \cdots & 0 & -1 & 1 \end{pmatrix}_{N_z \times N_z} ,$$

where a_i, b_i, c_i are the coefficients in the finite-difference scheme, $p_{i,j}$ the unknown pressure, N_z the grid number in the z direction, Δz the length of the grid cell, and $d_{i,j}$ the source term. The Neumann boundary condition has been applied to the first and last rows in matrix A, of which the eigenmatrixs are read as

$$AQ = \Lambda Q, \, GAQ = \Lambda = diag\{\lambda_j\},$$

$$Q = \{q_j\}, \, G = \{g_j\},$$

$$q_j = C_j \{\cos \frac{(j-1)\pi}{2N_z}, \cos \frac{3(j-1)\pi}{2N_z}, ..., \cos \frac{(2N_z-1)(j-1)\pi}{2N_z}\}^T , \tag{A2}$$

$$\lambda_j = 2 - 2\cos \frac{(j-1)\pi}{N_z}, \, C_j = \{ \begin{matrix} 1/N_z, \, j = 1 \\ 2/N_z, \, j \neq 1 \end{matrix} ,$$

$$g_j = \{1, \cos \frac{(2j-1)\pi}{2N_z}, \cos \frac{2(2j-1)\pi}{2N_z}, ..., \cos \frac{(N_z-1)(2j-1)\pi}{2N_z}\}.$$

Note that the products of G and Q can be executed with a staggered cosine-FFT. Then, by multiplying G to Eq. (A1), we can obtain

$$a_i \mathbf{Y}_{i-1} + b_i \mathbf{Y}_i + c_i \mathbf{Y}_{i+1} + \Lambda \mathbf{Y}_i = \mathbf{E}_i,$$

$$\mathbf{Y}_i = G\mathbf{X}_i, \, \mathbf{E}_i = G\mathbf{D}_i,$$

and the series of tridiagonal equations are

$$a_i y_{i-1,j} + b_i y_{i,j} + c_i y_{i+1,j} + \lambda_j y_{i,j} = e_{i,j}.$$

For j=1, the tridiagonal equations are singular and any additional restrict condition can be imposed, so the series of tridiagonal equations can be solved with the highly efficient Thomas algorithm.

[1] Z. Yin, P. Gao, W. R. Hu, and L. Chang, "Thermocapillary migration of nondeformable drops," Phys. Fluids **20**, 082101 (2008).

[2] N. O. Young, J. S. Goldstein, and M. J. Block, "The motion of bubbles in a vertical temperature gradient," J. Fluid Mech. **11**, 350–356 (1959).

[3] R. S. Subramanian and R. Balasubramaniam, *The Motion of Bubbles and Drops in Reduced Gravity* (Cambridge University Press, Cambridge, UK, 2001).

[4] R. Balasubramaniam and R. S. Subramanian, "The migration of a drop in a uniform temperature gradient at large Marangoni numbers," Phys. Fluids **12**, 733–743 (2000).

[5] H. Haj-Hariri, Q. Shi, and A. Borhan, "Thermocapillary motion of deformable drops at finite Reynolds and Marangoni numbers," Phys. Fluids **9**(4), 845–855 (1997).

[6] X. J. Ma, R. Balasubramaniam, and R. S. Subramanian, "Numerical simulation of thermocapillary drop motion with internal circulation," Numer. Heat Transfer, Part A **35**(3), 291–309 (1999).

[7] R. Balasubramaniam, C. E. Lacy, G. Woniak, and R. S. Subramanian, "Thermocapillary migration of bubbles and drops at moderate values of the Marangoni number in reduced gravity," Phys. Fluids **8**, 872–880 (1996).

[8] P. H. Hadland, R. Balasubramaniam, G. Wozniak, and R. S. Subramanian, "Thermocapillary migration of bubbles and drops at moderate to large Marangoni number and moderate Reynolds number in reduced gravity," Exp. Fluids **26**, 240–248 (1999).

[9] J. C. Xie, H. Lin, P. Zhang, F. Liu, and W. R. Hu, "Experimental investigation on thermocapillary drop migration at large Marangoni number in reduced gravity," J. Colloid Interface Sci. **285**, 737–743 (2005).

[10] P. T. Brady, M. Herrmann, and J. M. Lopez, "Confined thermocapillary motion of a three-dimensional deformable drop," Phys. Fluids **23**, 022101 (2011).

[11] G. Tryggvason, B. Bunner, A. Esmaeeli, D. Juric, and N. Al-Rawahi, "A front-tracking method for the computations of multiphase flow," J. Comput. Phys. **169**, 708–759 (2001).

[12] A. J. Chorin, "A numerical method for solving incompressible viscous flow problems," J. Comput. Phys. **2**, 12–26 (1967).

[13] B. Bunner, "Numerical simulation of gas-liquid bubbly flows," Ph.D. dissertation (The University of Michigan, 2000).

[14] B. L. Buzbee, G. H. Golub, and C. W. Nielson, "On direct methods for solving Poisson's equations," SIAM J. Numer. Anal. **7**, 627–656 (1970).

[15] P. Amodio and M. Aprzycki, "A cyclic reduction approach to the numerical solution of boundary value ODEs," SIAM J. Sci. Comput. **18**, 56–68 (1997).

[16] R. W. Hocknfy, "A fast direct solution of Poisson's equation using Fourier analysis," J. ACM **12**, 95–113 (1965).

[17] H. Shintani, "Direct solution of partial difference equations for a rectangle," J. Sci. Hiroshima Univ., Ser. A-1 **32**, 17–53 (1968).

[18] J. Englund and J. Helsing, "A comparison of splittings and integral equation solvers for a nonseparable elliptic equation," Bit Numer. Math. **44**, 675–697 (2004).

[19] L. Chang, Z. Yin, and W. R. Hu, "Transient behavior of the thermocapillary migration of drops under the influence of deformation," Scientia Sinica: Phys, Mech & Astron **41**, 960–968 (2011) (in Chinese); see the English version at e-print arXiv:1107.0519v2.

[20] R. Kronig and J. C. Brink, "On the theory of extraction from falling droplets," Appl. Sci. Res. **2**(1), 142–154 (1950).

[21] J. Glimm, J. W. Grove, X. L. Li, K. Shyue, Y. Zeng, and Q. Zhang, "Three-dimensional front tracking," SIAM J. Sci. Comput. **19**(3), 703–727 (1998).

[22] Y. Zhuang and X. H. Sun, "A high-order fast direct solver for singular Poisson equations," J. Comput. Phys. **171**, 79–94 (2001).

[23] H. Y. Wang, W. Jiang, and Y. N. Wang, "Parallelization and optimization of electrostatic particle-in-cell/Monte-Carlo coupled codes as applied to RF discharge," Comput. Phys. Commun. **180**, 1305–1314 (2009).